AERONET-based nonspherical dust optical models and effects on the VIIRS Deep Blue/SOAR over-water aerosol product

Jaehwa Lee[1,2], **N. Christina Hsu**[1], **Andrew M. Sayer**[1,3], **Corey Bettenhausen**[1,4], and **Ping Yang**[5]

[1]NASA Goddard Space Flight Center, Greenbelt, Maryland, USA

[2]Earth System Science Interdisciplinary Center (ESSIC), University of Maryland, College Park, Maryland, USA

[3]Goddard Earth Science Technology and Research (GESTAR), Universities Space Research Association, Columbia, Maryland, USA

[4]ADNET Systems Inc., Bethesda, Maryland, USA

[5]Department of Atmospheric Sciences, Texas A&M University, College Station, Texas, USA

Abstract

Aerosol Robotic Network (AERONET)-based nonspherical dust optical models are developed and applied to the Satellite Ocean Aerosol Retrieval (SOAR) algorithm as part of the Version 1 Visible Infrared Imaging Radiometer Suite (VIIRS) NASA 'Deep Blue' aerosol data product suite. The optical models are created using Version 2 AERONET inversion data at six distinct sites influenced frequently by dust aerosols from different source regions. The same spheroid shape distribution as used in the AERONET inversion algorithm is assumed to account for the nonspherical characteristics of mineral dust, which ensures the consistency between the bulk scattering properties of the developed optical models with the AERONET-retrieved microphysical and optical properties. For the Version 1 SOAR aerosol product, the dust optical models representative for Capo Verde site are used, considering the strong influence of Saharan dust over the global ocean in terms of amount and spatial coverage. Comparisons of the VIIRS-retrieved aerosol optical properties against AERONET direct-Sun observations at three island/coastal sites suggest that the use of nonspherical dust optical models significantly improves the retrievals of aerosol optical depth (AOD) and Ångström exponent by mitigating the well-known artifact of scattering angle dependence of the variables observed when incorrectly assuming spherical dust. The resulting removal of these artifacts results in a more natural spatial pattern of AOD along the transport path of Saharan dust to the Atlantic Ocean; i.e., AOD decreases with increasing distance transported, whereas the spherical assumption leads to a strong wave pattern due to the spurious scattering angle dependence of AOD.

Corresponding author: Jaehwa Lee (jaehwa.lee@nasa.gov).

1 Introduction

Mineral dust, among other aerosol types, is one of the key constituents in the terrestrial atmosphere, producing important climate forcing through directly perturbing radiation balance [*Liao and Seinfeld*, 1998; *Li et al.*, 2004; *Lee et al.*, 2014] and interacting with clouds [*Yin et al.*, 2002; *Yoshioka et al.*, 2007; *Cziczo et al.*, 2013]. It contributes to a significant portion of the global aerosol loadings thereby responsible for a large amount of the aerosol radiative effect [*Tegen et al.*, 1997; *Chin et al.*, 2014].

One of the important characteristics of mineral dust particles from light scattering perspective are their nonspherical geometric shape, which makes the Lorenz-Mie theory inappropriate for the calculation of their scattering properties. To overcome this issue, numerous efforts have been made to accurately compute the light scattering of nonspherical particles, including the T-matrix method [*Waterman*, 1971; *Mishchenko and Travis*, 1994], the discrete dipole approximation [*Draine and Flatau*, 1994; *Yurkin et al.*, 2007], the finite-difference time domain method [*Yee*, 1966; *Yang and Liou*, 1995, 1996; *Yang et al.*, 2000], and geometric optics method [*Yang et al.*, 2007; *Bi et al.*, 2009]. Each methodology has different advantages and disadvantages in terms of computational time, and applicable particle morphology and size regimes.

Although spheroid mixtures [e.g. *Mishchenko et al.*, 1997] are not representative for 'real' dust in terms of geometric shape, they mimic the scattering and absorption characteristics of realistic dust particles reasonably well if appropriate refractive indices and shape distribution are used [*Dubovik et al.*, 2006; *Kemppinen et al.*, 2015]. Consequently, spheroid mixtures have been used in aerosol inversion algorithms for ground-based and spaceborne instruments given the fact that it is impractical to implement ever-changing dust morphologies in the algorithms [*Kahn et al.*, 1997; *Dubovik et al.*, 2006; *Feng et al.*, 2009; *Lee et al.*, 2012].

Since aerosols are ubiquitous and show complex spatiotemporal distributions over the globe, satellite observations have been recognized as an important source of data, with the ability to observe extensive areas at a high spatiotemporal resolution [*Kaufman et al.*, 2002]. Satellite algorithms to retrieve aerosol optical properties using visible to shortwave infrared bands generally incorporate lookup tables of calculated TOA (top of the atmosphere) reflectance for various aerosol types (or aerosol optical models) to compare the simulated TOA reflectance against the measurements made by the satellite sensors in their retrieval implementations. Therefore, the simulation of the TOA reflectance needs to be highly accurate, and thus demands realistic aerosol optical property models in the radiative transfer calculations.

As one of the NASA's operational aerosol retrieval algorithms, the Deep Blue aerosol project (https://deepblue.gsfc.nasa.gov) has provided long-term global aerosol data records over both land and water surfaces using Sea-viewing Wide Field-of-view Sensor (SeaWiFS) from 1997 to 2010 [*Hsu et al.*, 2004, 2006, 2013; *Sayer et al.*, 2012a, 2012b] and over land using the twin Moderate Resolution Imaging Spectroradiometer (MODIS) sensors aboard Terra from 2000 onwards and Aqua from 2002 onwards [*Hsu et al.*, 2013; *Sayer et al.*, 2013, 2014, 2015]. The Deep Blue algorithm is renowned for its application to bright land surfaces

such as desert, which is accomplished by the use of blue bands (412 and 470 nm for MODIS or 490 nm for SeaWiFS) in the retrieval process. With the launch of the Suomi National Polar-orbiting Partnership (S-NPP) satellite in late 2011, the algorithm now extends its application to the measurements made by the Visible Infrared Imaging Radiometer Suite (VIIRS) instrument to continue the Deep Blue aerosol data record beyond the Earth Observing System era. Like SeaWiFS, the VIIRS Deep Blue will produce data over both land and water surfaces as retrieved by the enhanced Deep Blue [*Hsu et al.*, 2013] and Satellite Ocean Aerosol Retrieval (SOAR) algorithms [*Sayer et al.*, 2017], respectively.

The Deep Blue algorithm applied to land surfaces includes a nonspherical dust optical model with an empirical phase function that well matches the AERONET-derived dust phase function in backscattering direction [*Hsu et al.*, 2004]. However, the prior application of SOAR only incorporated spherical dust, which resulted in biases in aerosol properties over regions where dust aerosols are frequently observed. It is well known that the spherical assumption leads to an unrealistic scattering angle dependence of aerosol optical depth (AOD) (as well as Ångström exponent) mainly due to poor representation of the shape of the phase function [*Masuda et al.*, 2002; *Levy et al.*, 2003; *Mishchenko et al.*, 2003; *Wang et al.*, 2003; *Lee et al.*, 2012; *Banks et al.*, 2016]; i.e., it results in an overestimation in the side-scattering direction ($80° < \Theta < 150°$) and an underestimation in the backscattering direction ($\Theta > 150°$) with a bias as high as 50%.

The foci of the present study are to develop nonspherical dust optical models for SOAR, to analyze the effects of the new optical models on the aerosol retrieval performance, and to provide a further practical illustration of the type of artifacts which can arise from the assumption of spherical dust in satellite remote sensing algorithms. Although the results are illustrated for the application to SOAR and VIIRS data, these optical models are more broadly applicable to any aerosol property retrieval. Section 2 summarizes the data and methodology used, and section 3 addresses dust optical models developed for SOAR. In section 4, the effects of the nonspherical dust optical model on retrieval performance are discussed. Finally, the major findings of this study are summarized in section 5.

2 Data and Methods

2.1 AERONET direct-Sun and inversion data

Aerosol Robotic Network [AERONET, *Holben et al.*, 1998] direct-Sun and inversion products are used to develop dust optical models for use in the SOAR algorithm and validate the SOAR-retrieved aerosol products. We only consider cloud-screened and quality-assured Level 2 products to minimize potential errors due to cloud contamination and other error sources [*Dubovik et al.*, 2000; *Smirnov et al.*, 2000; *Holben et al.*, 2006]. The main purpose of the direct-Sun measurements is to provide spectral AOD (τ_λ; where λ is wavelength) at multiple wavelengths ranging from 340 to 1640 nm. The wavelength range and number of channels within the range vary with the sites (440, 675, 870, and 1020 nm being standard). Data are provided at a temporal resolution of ~5 – 15 min with an AOD uncertainty of 0.01 – 0.02 [*Holben et al.*, 1998; *Eck et al.*, 1999]. Ångström exponent (hereafter denoted as AE or α), a qualitative indicator of aerosol particle size [*Ångström*, 1929], can be derived as the slope of spectral AOD across a certain wavelength range on a logarithmic scale,

$$\alpha = -\frac{\ln(\tau_{\lambda 1}) - \ln(\tau_{\lambda 2})}{\ln(\lambda 1) - \ln(\lambda 2)}. \quad (1)$$

In this investigation AERONET α is defined across the spectral range 440 – 870 nm.

The AERONET inversion algorithm [*Dubovik and King*, 2000; *Dubovik et al.*, 2006] makes use of sky radiance observations in the solar almucantar in combination with direct-Sun data to retrieve the microphysical and optical properties of aerosols, which are required to calculate their bulk scattering properties (as opposed to single-scattering properties for individual particles). The bulk scattering properties include spectral AOD, the single-scattering albedo (SSA), and the phase function (or the phase matrix for vector radiative transfer model), which are the key parameters needed for radiative transfer calculations. The inversion data include aerosol size distribution, spectral complex refractive indices at four wavelengths, and percentage of scattering arising from spherical particles (also known as "sphericity parameter"), retrieved as best matching the observed sky radiances in a wide scattering angle range ($2°$ – $2 \times$ solar zenith angle), given spectral AOD observed by the direct-Sun measurement.

The size distribution is binned at 22 logarithmically-spaced radii ranging from 0.05 – 15 μm. Then, the size distribution parameters, including volume concentration (C_v), volume median radius (r_v), geometric standard deviation (σ), and effective radius (r_{eff}), can be derived from the retrieved size distribution. Although AERONET does not impose a distribution shape, these parameters are often used to define a bimodal lognormal volume size distribution,

$$\frac{dV(r)}{d\ln r} = \sum_{i=1}^{2} \frac{C_{v,i}}{\sqrt{2\pi}\sigma_i} e^{-\frac{1}{2}\left(\frac{\ln r - \ln r_{v,i}}{\sigma_i}\right)^2}. \quad (2)$$

Note that in the AERONET inversion, the fine and coarse modes are separated at the inflection point within the size interval 0.439 – 0.992 μm, and the size distribution parameters are provided for each mode. The effective radius is defined as the ratio of the third to second moments of the number size distribution, which represents mean particle radius weighted by projected area, as first introduced by Hansen and Travis (1974) in the form,

$$r_{eff} = \frac{\int_{r_{min}}^{r_{max}} r^3 \frac{dN(r)}{d\ln r} d\ln r}{\int_{r_{min}}^{r_{max}} r^2 \frac{dN(r)}{d\ln r} d\ln r}. \quad (3)$$

Although the size distribution and effective radius of nonspherical particles can be represented by more generalized forms, Eqs. (2) and (3) are used in the AERONET inversion, as it assumes volume-equivalent spheres for nonspherical particles [*Dubovik et al.*, 2006].

Both the real and imaginary parts of the refractive index are provided at the four wavelengths (440, 675, 870, and 1020 nm), assuming a single refractive index representative for the whole size distribution range. Note that, while this may cause issues in the case where both fine and coarse modes of different compositions contribute significantly to the total AOD, but in the case of dust aerosols the coarse mode is typically optically dominant and the aforementioned issue is much less concerned. The wavelength- and size mode-independent sphericity parameter (100% – nonsphericity parameter) describes the degree of aerosol nonsphericity, as it represents the relative contributions of spherical and nonspherical particles to the final bulk scattering properties, given microphysical and optical properties retrieved. A fixed spheroid shape distribution is assumed for the nonspherical component (see Fig. 13 in *Dubovik et al.*, 2006).

2.2 Aerosol single-scattering property database

Since AERONET inversions only provide aerosol bulk scattering properties at selected wavelengths (and also do not provide the full phase matrix), they must be extended to VIIRS wavelengths to create the lookup tables for the SOAR algorithm. To this end, we incorporate a single-scattering property database for individual ellipsoidal particles (including spherical and spheroidal particles) developed by *Meng et al.* [2010]. This saves tremendous computational time that is required for calculating the single-scattering properties of spheroids for wide ranges of particle sizes and aspect ratios. The databases were created by employing four different computational methods for different particle size parameter and shape regimes: Mie theory [*Bohren and Huffman*, 1983] for spherical particles, T-matrix method [*Mishchenko et al.*, 1997] and discrete dipole approximation [*Yurkin et al.*, 2007] for spheroidal and ellipsoidal particles with small-to-moderate size parameters (up to 20 – 40), respectively, and an improved geometric optics method [*Yang et al.*, 2007; *Bi et al.*, 2009] for ellipsoidal particles (including spheroids) with large size parameters (higher than 10 – 20).

The database takes in inputs that cover wide ranges of size parameters (0.025 – 1000), refractive index (1.1 – 2.1 for the real part and 0.0005 – 0.5 for the imaginary part), and two aspect ratios (0.3 – 1 describing deformation of spheres in both semi-major and semi-minor axes), which are useful for various applications and cover the range of values expected for terrestrial aerosol remote sensing/modeling [e.g. *Lee et al.*, 2012; *Colarco et al.*, 2014; *Buchard et al.*, 2015; *Kemppinen et al.*, 2015]. A software package is also included in the database to provide interpolated results in the case that the microphysical and optical parameters are provided between the database node points, and to generate bulk scattering properties integrated over certain particle size and shape distributions. Among other outputs, we use the phase matrix, and extinction and scattering efficiencies of individual particles to create bulk scattering properties for dust size distributions that will be derived later in this work, given the AERONET's spheroid shape distribution.

Figure 1 shows an example of bulk scattering properties (AOD, SSA, and phase function) from AERONET superimposed with those from the database assuming spherical particles and sphere/spheroid mixtures as a function of the sphericity parameter (hereafter, "sphere/spheroid mixture" will be referred to as simply "spheroid" for brevity). A severe dust event observed at Capo Verde with the sphericity parameter of 0.69% was chosen. It is found that the database accurately produces the AERONET-retrieved spectral AOD (generally within 1%), SSA (within 3% or better depending on wavelength), and the phase function (within 0.05 for scattering angles > 30°; note VIIRS and most other spaceborne sensors generally observe scattering angles in the range ~80°-180°). The spherical assumption results in larger differences than the spheroid case, particularly in the phase function, demonstrating possible scattering angle-dependent errors in the satellite-retrieved aerosol optical properties for dust-laden cases. The slight differences observed for the spheroid case are likely due to the difference in handling the size distribution when integrating the single-scattering properties (trapezoidal approximation for AERONET inversion [*Dubovik et al.*, 2006] vs. linear interpolation in this study). The difference in the single-scattering property databases used, i.e., different node points for size parameter, refractive index, and aspect ratio between AERONET inversion and this study, can also cause slightly differences in the final bulk scattering properties due to the errors caused by interpolations between the node points.

2.3 SOAR algorithm for VIIRS

Here we provide a brief description of the VIIRS SOAR algorithm and its data products. The initial application to SeaWiFS was described fully by *Sayer et al.* [2012b]; information on the VIIRS application can be found in *Sayer et al.* [2017], and a full description of the VIIRS application will be provided in a follow-up study.. SOAR provides aerosol optical properties including AOD and fine-mode AOD fraction (FMF) at 550 nm, 440-870 nm AE, aerosol type (marine, fine-dominated, or dust), and spectral AOD (at 488, 555, 672, 865, 1240, 1610, and 2250 nm). The data products are provided at a nominal spatial resolution of 6 km × 6 km (8 × 8 pixel aggregation) at the sub-satellite point over cloud- and snow/ice-free water surfaces. The inversion procedure to convert the TOA reflectances measured by VIIRS into aerosol optical properties incorporates lookup tables calculated for three aerosol optical models for different AOD and FMF (both at 550 nm) regimes: marine model for AOD range 0.001 – 0.25 and FMF range 0.0 – 0.9, fine-dominated model for AOD range 0.15 – 5.0 and FMF range 0.7 – 1.0, and dust model for AOD range 0.15 – 5.0and FMF range 0.0 – 0.6. The minimization procedure tests the χ^2 statistic between observed and calculated TOA reflectances to simultaneously retrieve AOD and FMF and to find best aerosol optical model out of the three. No mixing between the optical models is assumed.

The dust optical model is developed in a way to minimize changes in the algorithm (and lookup table) structure of SOAR (i.e., separated from other optical models as no combination between models are assumed). In addition, it has flexibility to include different fine-mode component when necessary. Sayer et al. [2014] suggested that biomass burning smoke aerosols from different sources and burning types can show significantly different optical properties from one another and also from the fine-dominated optical model assumed in the SOAR algorithm. This has implications that AOD biases over certain regions can be due to this variety of optical properties and thus can be reduced if more appropriate aerosol

models are used. For future implementation of this variety, bulk scattering properties of fine-and coarse-mode are created separately under the assumption of bimodal lognormal size distribution, and are combined as a function of FMF for the bulk scattering properties. This facilitates future creation of dust optical models mixed with various fine-mode aerosols, such as urban pollution and biomass burning smoke from various sources. In addition, when creating optical models with intermediate FMF, we can avoid using the inversion data for fine/coarse mixed conditions, for which the inversion data are thought to be less accurate due to the assumption of homogeneous particles (i.e., a single refractive index for particles of all sizes) [*Dubovik and King*, 2000].

3 Creating Dust Optical Models for SOAR

We derive the microphysical and optical properties of coarse-mode dust from different source regions based on AERONET inversion data. The properties are then used for obtaining bulk scattering properties through the single-scattering property database, which will eventually be used in creating the dust lookup table for SOAR.

3.1 Microphysical and optical properties of dust as seen by AERONET

To analyze microphysical and optical properties of dust-dominated aerosols, global AERONET inversion data are filtered first for FMF (550 nm) < 0.2, coarse-mode AOD (550 nm) > 0.5, and sphericity parameter < 1%. The choice of these thresholds is to minimize the effects of fine-mode aerosols that are chemically different from dust (small FMF), the uncertainty in the inversion algorithm (high AOD), and non-dust coarse-mode aerosols (low sphericity) on the inversion products for dust properties while maintaining sufficient number of data points [cf. *Dubovik et al.*, 2000; *Lee et al.*, 2012; *Schuster et al.*, 2016]. Although these thresholds are somewhat subjective, variations within a reasonable range only negligibly affect the resulting models. Then, medians are used to represent the dust aerosols observed at each AERONET site, to reduce the sensitivity to anomalous conditions or AERONET retrieval errors.

Figure 2 shows a large-scale view of dust microphysical and optical properties at locations where dust aerosols, defined by the above filters, are frequently observed (number of data points > 30). The median coarse-mode effective radius suggests larger particle sizes over India and China than over North Africa and the Arabian Peninsula, possibly due to differences in transport distance and wind speed [*Kok*, 2011]. It is worthwhile to note that a decreasing tendency of particle size of dust generated in the Bodélé Depression (decreasing effective radius from east to west over North Africa) is detected during the transport likely due to faster dry deposition of larger particles [*Giorgi*, 1986; *Lin et al.*, 1994]. In addition, the smaller effective radii in the coastal regions imply that using data from inland AERONET sites for ocean algorithm could lead to an overestimation of particle size, which can in turn result in an overestimation in the satellite-retrieved AOD due to an underestimation in the aerosol backscattering fraction (the larger the particle size, the lower the backscattering fraction).

The SSA at 440 nm, where strong absorption by mineral dust occurs, generally ranges from 0.87 to 0.93, showing a minimum of ~0.875 at Xianghe, China. The low SSA at Xianghe is

mainly due to the effect of the reddish (as opposed to whitish) dust (strong absorption in blue wavelength) from Inner Mongolia as well as possible internal mixing with carbonaceous aerosols [*Scarnato et al.*, 2015; *Sugimoto et al.*, 2015]. The maxima of ~0.925 at Mezaira, Abu Dhabi and Karachi, Pakistan are associated with the relatively bright (whitish) dust from southeastern Arabian Desert [e.g. *Eck et al.*, 2008] and both transported Arabian dust and dust from local sources in Pakistan and Afghanistan [e.g. *Alam et al.*, 2011], respectively. Aside from the two extremes, 440 nm SSA are generally within the range of 0.89–0.91, suggesting that 440nm SSA of 0.90 can be a reasonable first guess for satellite algorithms.

The asymmetry parameter g (cosine-weighted mean of phase function) by definition represents the degree of deviation of scattering from the forward direction, varying from −1 (pure backward scattering) to 1 (pure forward scattering). It is one of the factors determining direct radiative effects of aerosols. From light scattering theory, g depends on particle size (larger particle corresponds to higher g) and refractive index (higher real/imaginary part of the refractive index correspond to lower/higher g, respectively). It shows higher values in North Africa than Asia, demonstrating the real part of the refractive index being stronger than effective radius at controlling the g, which is likely due to the small differences in the effective radii between the sites. Although the complex refractive index is determined by chemical composition of mineral dust, geometric shapes can also be a factor that changes the apparent refractive index, as the AERONET inversion assumes a fixed spheroid shape distribution in the retrieval process [cf. *Kemppinen et al.*, 2015].

Figure 3 shows the microphysical and optical properties of dust at six distinct locations (Capo Verde, Solar Village, Mezaira, Kanpur, SACOL; Semi-Arid Climate Observatory, and Xianghe), for which dust optical models are created. The locations are selected to represent dust from different source regions; i.e., Saharan dust for Capo Verde, Arabian dust from different regions for Solar Village and Mezaira, dust from Thar Desert for Kanpur, from Taklimakan and Gobi Desert for SACOL, and from Taklimakan, Gobi, and Inner Mongolia for Xianghe. It is revealed that despite the different sources, some of the properties are similar between different locations, such as the binned volume size distributions peaking at 2.24 μm (with some differences in geometric standard deviations) and rather flat spectral AOD due to coarse-mode optical dominance. However, the 440 nm SSA (and corresponding imaginary part of the refractive index), asymmetry parameter, and the real part of the refractive index denote different optical characteristics of dust from different source regions. The range of SSA for different sites decreases with wavelength, and is only ~0.01 at 870 and 1020 nm. This indicates possible use of a simple SSA assumption for the longer wavelengths. The asymmetry parameter generally decreases with wavelength and flattens for wavelength > 675 nm, still showing strong forward scattering even at the longer wavelengths (g > 0.7). The real part of the refractive index generally decreases with wavelength in a magnitude of ~0.04, and the imaginary part, which is highly related to SSA, shows a wide range (0.0027 – 0.0044) at 440 nm and lower values with narrower ranges (0.0007–0.0012) at the longer wavelengths.

We assume that the refractive index of the dust-dominated cases represents coarse-mode dust properties (i.e. the small contribution from the fine-mode for these cases does not

significantly affect the average retrieved refractive index). For size distribution, we use AERONET-derived size distribution parameters for coarse-mode (volume median radii and geometric standard deviations) rather than the median size distributions itself, as we intend to create coarse-mode only dust optical models, and the small volume concentrations of the fine-modes (Figure 3a) can make the inflection point separating fine- and coarse-modes ambiguous for the dust-dominated cases. For fine-mode, the same fine-mode optical model used in SOAR for fine-dominated model [*Sayer et al.*, 2012b] is adopted but with reduced imaginary part of the refractive index (from 0.0075 to 0.001). This is to account for the lower imaginary part of the refractive index derived from AERONET for dust-dominated cases (0.0027-0.0044 for 440 nm and 0.0007-0.0014 for $\lambda \geq 675$ nm). Tables 1 and 2 summarize the microphysical and optical properties of coarse-mode dust at the six locations and those of fine-mode, respectively.

3.2 Bulk scattering properties of dust optical model

Given the size distribution parameters and complex refractive index in Tables 1 and 2, we derive bulk scattering properties by integrating the single-scattering properties of individual particles over the size distribution for fine-mode (spheres) and both size distribution and aspect ratio for coarse-mode (spheroids). As mentioned previously, we assume the same spheroid shape distribution as used in the AERONET inversion algorithm for the coarse-mode (dust), such that the optical model can be consistent with the sky radiance measurements made by AERONET. The fine- and coarse-mode optical models are created separately and then mixed together in the radiative transfer model (VLIDORT; *Spurr*, 2006) for calculating the lookup table for the various FMF values (0.0 – 0.6 with an increment of 0.1). The integration is performed for logarithmically distributed node points; 1000 size parameter nodes between 0.03 and 999 for the fine-mode; 100 size parameter nodes between 0.03 and 999 and 9 reciprocal aspect ratio nodes between 0.3349 and 0.6944 for prolate and oblate particles for the coarse-mode. This integration node density is sufficient to avoid artificial oscillations in the calculated phase matrix elements resulting from lack of convergence. Then, spectral extinction coefficient, SSA, and phase matrix are used for the radiative transfer calculations. For SOAR Version 1 data processing, we assume dust properties representative for Capo Verde site for the coarse-mode, considering the significant contribution of the Saharan dust over the global ocean in terms of amount and spatial coverage. Future versions of the SOAR/Deep Blue product may consider additional dust optical models.

Figure 4 shows medians and central 68% intervals of the bulk scattering properties (spectral AOD relative to 550 nm, SSA, and asymmetry parameter representative of the phase function) of the dust optical model together with those derived from AERONET inversion data at the six locations, for various FMF ranges. The bulk scattering properties of the optical model are calculated by combining the values of the fine- and coarse-mode according to FMF of the individual inversions from all of the AERONET sites used. The comparisons suggest that the dust model represents the dust properties from various source regions well, generally showing intermediate values, although it is based only on Capo Verde input data (Figure 4a–4c). This is likely due to the use of the separate fine-mode optical model of which microphysical and optical properties are different from those of Capo Verde and

partly due to the fixed size distribution used. The uncertainty in FMF in the inversion data arising from the determination of the inflection point in the retrieved size distribution [cf. *O'Neill et al.*, 2003] can also affect the spectral features, but it does not seem to be a significant factor here. The dust model, as expected, has weaknesses in reproducing optical properties, particularly SSA, for the higher FMF regime (Figure 4k) due to increased influences of fine-mode aerosols with various optical properties depending on locations [e.g. *Dubovik et al.*, 2002], as well as decreased performance of AERONET inversion data for fine/coarse mixed conditions. This discrepancy can be reduced by including more absorbing fine-mode model such as the one used in the SOAR for fine-dominated aerosols [*Sayer et al.*, 2012b] or even more absorbing ones suggested by Sayer et al. [2014]. This will be a subject of future study once error characteristics of VIIRS SOAR product have been examined through a long-term global evaluation of the data set. It should be noted that FMF of dust is typically lower than 0.4 (although severe anthropogenic aerosol event mixed with dust can increase the value) [cf. *Dubovik et al.*, 2002; *Eck et al.*, 2010], and fine-dominated model instead of dust is used for FMF > 0.6, such that the impact of using the weakly absorbing fine-mode for the dust optical model can be insignificant.

3.3 Extension to VIIRS wavelengths and fine-tuning for optimal performance

Since the complex refractive indices from AERONET inversion are limited to wavelength range 440 – 1020 nm, they must be somehow extended to the relevant VIIRS bands (seven bands centered at 488, 555, 672, 865, 1240, 1610, and 2250 nm). The extension for the fine-mode can be done relatively easily because (1) we assume fixed refractive index within the AERONET wavelength range (thus the same real and imaginary values can be used for the VIIRS bands within the range), and (2) contribution of fine-mode aerosols to TOA reflectance is small at the longer wavelengths ($\lambda > 1020$ nm) (thus change in refractive index has marginal impact at the longer wavelengths). As a result, we assume the same imaginary part of the refractive index throughout the VIIRS bands, and slightly reduced real part of the refractive index for $\lambda > 1020$ nm, according to the water-soluble aerosol component at 70% relative humidity introduced in *Hess et al.* [1998].

The extension for coarse-mode, however, should be handled carefully because both real and imaginary parts of the refractive index vary within the AERONET wavelength range, and are expected to change outside the range as well. In addition, it has strong effects on TOA reflectance even at longer wavelengths due to the large particle size. It is well known that the imaginary part of the refractive index of dust increases (SSA decreases) towards ultraviolet (UV) wavelengths while showing small values (SSA generally higher than 0.95 based on AERONET inversions) for $\lambda > \sim600$ nm, as iron oxides in dust particles significantly absorb radiation in UV through mid-visible wavelength range [*Gillespie and Lindberg*, 1992; *Sokolik and Toon*, 1999]. *Wagner et al.* [2012] suggest that the increase in the imaginary part of the refractive index with decreasing wavelength can be characterized by a linear fit in both linear and logarithmic scale. Accordingly, a linear interpolation/extrapolation in logarithmic scale is assumed for the imaginary part of the refractive index while restraining the values higher than 0.0005 to keep the value within the range that the single-scattering property database can handle. For real part, a linear interpolation within 440 – 1020 nm and slightly reduced values for $\lambda > 1020$ nm are used according to the spectral shape of feldspar

particles [*Egan and Hilgeman*, 1979; *Smith and Grainger*, 2014], which is the most abundant mineral group on Earth and is used as validation target for the AERONET inversion algorithm.

Finally, the real and imaginary parts of the refractive index are increased and decreased by 5% and 40%, respectively. Final values used in SOAR are shown in Table 3. These adjustments are semi-empirical and improve the agreement with independent AERONET direct-Sun AOD/AE data. The real parts of the refractive indices remain in-family, while the imaginary counterparts decrease somewhat; however, the magnitudes are reasonable as they are smaller than the level of uncertainties in AERONET refractive index [*Dubovik et al.*, 2000, 2006], i.e. ±0.04 and ±50% for real and imaginary parts respectively. While empirical adjustments are best avoided where possible, the AERONET inversions have some limitations which can lead to suboptimal performance when results are applied to different studies. Of particular relevance to the present study are that:

1. The current version 2 inversions use a scalar radiative transfer code (rather than a vector code like VLIDORT). Scalar codes lead to biases in simulations of absorbing aerosols, such as dust [e.g. *Levy et al.*, 2004]. A future AERONET version 3 will use a vector code [S. Korkin/A. Sinyuk, personal communication, 2017], which should remove this error source.

2. The spheroidal aspect ratio distribution used by the AERONET team is itself empirical, as it was optimized to match observations of real dust (which is neither spherical nor truly spheroidal) phase functions in the midvisible spectral region [*Dubovik et al.*, 2006]. The resulting particle shape distribution, which is also adopted in the current study, may therefore be less appropriate for simulations of dust at longer wavelengths. In this regard, adjusting the assumed refractive indices at these wavelengths can ameliorate these errors.

3. As noted earlier, AERONET assumes particles of all sizes to have the same refractive index, even though they may be of chemically distinct origins. In the present study the influence of this assumption was reduced by filtering AERONET inversions based on FMF to isolate dust-dominated scenes, although it could still be a factor.

Thus, while the AERONET inversions provide an excellent baseline from which to start, it is reasonable to make adjustments within this magnitude to improve the agreement with validation data (the AERONET direct-Sun data being independent of the AERONET inversions). It is hoped that revisiting the analysis with a future AERONET version may reduce or remove the extent to which empirical adjustments are necessary.

4 Effects of New Dust Optical Model on SOAR Aerosol Product

4.1 Validation against AERONET

VIIRS SOAR retrievals are evaluated at Capo Verde, Gosan (South Korea), KAUST Campus (Saudi Arabia), Karachi (Pakistan), and Lampedusa (Italy) AERONET sites where dust events are observed to greater or lesser extents. To this end, a spherical dust optical model (and lookup table) is also created using the same microphysical and optical properties as the

spheroidal counterpart except for the particle shape. The SOAR retrievals between spheroidal and spherical dust optical models are then compared to examine the effects of the new optical models on the retrieval performance. We only consider the quality-assured Level 2 aerosol product (quality flag = 3) for VIIRS, and the VIIRS data within 25 km of AERONET sites and AERONET data within ±30 min of VIIRS overpass time are averaged and compared. AERONET AOD is interpolated to 550 nm using the spectrally-closest wavelength and AERONET AE, which introduces negligible additional uncertainty. This has been the standard validation protocol for SOAR and many other satellite aerosol data products [e.g. *Sayer et al.*, 2012b, and references therein]. Note that the full SOAR algorithm is run, in which the retrieval selects the best-fitting aerosol optical model and there is no regional tuning. Thus, the retrieval is not forced to choose the dust model for these comparisons.

Tables 4 and 5 summarize the comparison statistics of AOD at 550 nm and AE, respectively, at the five locations. There are unfortunately only a limited number of AERONET coastal/island sites in dust-dominated areas available in the S-NPP era; those chosen cover several different dust aerosol source/transport regions. A forthcoming companion paper which describes the implementation of SOAR to VIIRS will include more validation results against global ship-based AOD measurements, including some dust areas. The comparison results reveal better performance of the spheroidal optical model than the spherical counterpart for these sites. Depending on site, for AOD (AE), the Pearson coefficient increases from 0.76 – 0.93 (−0.02 – 0.71) for spherical model to 0.90 – 0.98 (0.52 – 0.80) for spheroidal model, the root-mean-square error (RMSE) decreases from 0.05 – 0.16 (0.34 – 0.50) to 0.04 – 0.13 (0.21 – 0.39), and the fraction within the expected error (EE, ±0.03±10% for AOD) increases from 42% – 80% to 49% – 83%. Note that the EE refers to a confidence interval in which one standard deviation (~68%) of points are expected to lie with respect to a ground truth. This concept is the same as in other applications of SOAR and Deep Blue, and its values come from a combination of retrieval simulations and experience with similar algorithms and sensors [e.g. *Sayer et al.*, 2012a,b, 2013, 2014, 2015, 2017]. Thus, the target value overall for agreement within EE is ~68%; significantly more indicates retrieval errors are significantly smaller than expected, and vice versa.

For AOD, the median bias (MB) does not show significant differences between the two models likely due to cancelation of positive and negative biases when averaging. This implies that climatological AOD from the spherical model might not be significantly different from those of spheroidal model, although it is not immediately clear how long a data record must be aggregated to acquire unbiased results for the spherical model. Note that the smaller improvements at Gosan, Lampedusa, and Karachi than Capo Verde and KAUST Campus are associated with the smaller number of dust events for the former two sites, and local aerosol sources for Karachi (it is located in farther inland, and in a city of over 9 million people). The spheroidal model still slightly improves data quality at these locations where dust is less frequent (Gosan and Lampedusa); this also implies that the new dust model does not lead to a decreased performance for non-dust cases, for instance by choosing wrong aerosol model in the retrieval process.

Figure 5 shows scatterplots of AOD and AE at Capo Verde for which the current dust optical model was created (thus, potentially showing the best results). Because other sites show similar patterns, the same conclusions can be applied to them as well. First of all, we see that the small difference in AOD MB between spherical and spheroidal models is indeed due to cancelation of positive and negative errors when averaging. The scatterplot for spherical model demonstrates larger scatter, with weak overestimation of a larger number of data points and strong underestimation of a smaller number of data points, which resulted in a small positive MB of 0.02. Next, it seems that the spherical dust model works reasonably well for AOD of 0 to about 0.25 or 0.30, because in this AOD regime dust is likely mixed with spherical marine and/or other background aerosol types. Finally, the impact of using the spheroidal dust optical model is significant for AE, which implies that inaccurate FMF retrievals (as well as unrealistic phase function) from using the spherical assumption can exacerbate the biases in spectral AOD. This is consistent with other studies [e.g. *Levy et al.* 2003; *Remer et al.*, 2005; *Banks et al.* 2016].

To further examine the effects of the spheroidal dust optical models, Figure 6 illustrates the retrieval errors as a function of scattering angle and AE (as a proxy of dust fraction, i.e., lower AE corresponds to higher dust fraction). We find that the spheroidal optical model effectively mitigates the well-known scattering angle dependence of AOD (positive bias in the side-scattering direction and low negative in the backscattering direction) of the spherical assumption. The spheroidal model results in a slight positive bias regardless of scattering angle, which is likely related to the slight positive bias in AE (Figure 5d). Although the bias can be further improved by adjusting the mode radius and/or refractive index of the coarse-mode dust optical model, additional adjustment is not made as the single optical model is used for dust over the global water surfaces in this version of the algorithm.

The results as a function of AE reveal that the spherical model leads to a larger AOD scatter in lower AE regime (AE < 0.3) due to an inaccurate representation of dust phase function (and particle size), which is significantly improved in the case of the spheroidal model. The increasing positive bias with decreasing AE for the spheroidal model case implies a limitation of the fixed size distribution and refractive index of the dust optical model. As it is not clear how accurately the changing microphysical and optical properties can be modeled as a function of various parameters (AOD, transport distance, etc.), further investigations are underway.

4.2 Spatial distribution

The scattering angle dependence of AOD resulting from the spherical assumption creates an artificial spatial pattern in AOD maps, since the scattering angle changes significantly with the satellite viewing geometry. For satellite sensors in Sun-synchronous orbits such as VIIRS, the scattering angle, thus AOD bias, depends heavily on the cross-track scan angle, causing a characteristic east-west pattern of AOD. At low to mid-latitudes the largest scattering angle occurs near the sub-satellite point, slightly shifted toward east side of the scan for VIIRS, and it decreases with increasing scan angle in both directions. Therefore, AOD retrieved using a spherical dust optical model can show an artificial wave-like pattern due to the scattering angle change.

Figure 7 shows an example of the artificial spatial pattern for a dust event observed on 17 July 2012, which is significantly lessened with the use of the spheroidal optical model. As inferred from the scattering angle dependence of AOD, the spherical assumption leads to a significant underestimation of AOD (as high as 0.5 or 50%) in the eastern part of the Sun glint region, which occurs near the sub-satellite point shifted toward west, and a less significant overestimation (~0.1 or 20%) in the western part of Sun glint due to smaller difference in the phase function between the spherical and spheroidal dust optical models (Figure 7c). This creates a sudden dip and jump in AOD before and after crossing the sun glint region, causing an unnatural wave pattern in AOD. As inferred from Panels b and d in Figure 7, the spheroidal model creates a more natural AOD gradient along the transport path of the Saharan dust (AOD decreasing with transport distance), which has implications for satellite-based dust transport studies [e.g. *Yu et al.*, 2013].

While Figure 7 shows angular artifacts from the spherical assumption on an instantaneous basis, it is relevant to consider whether such artifacts persist in temporally-aggregated data. Monthly mean AOD shown in Figure 8 suggests that the spherical model leads to nonnegligible biases up to 25% as compared to the spheroidal model, although the absolute error is much smaller than the instantaneous case. In this specific case, the biases seem to exacerbate the inherent wave pattern in AOD, as the spherical assumption tends to overestimate (underestimates) AOD over regions with high (low) AOD. This implies that monthly means, which are frequently used for various scientific applications, might not be sufficient for these biases from spherical assumption to cancel out. In addition, it is not clear to what extent aggregations over longer periods of time will improve the bias. It should be noted that the spheroidal model does not fully eliminate the wave pattern, which arises as a result of sampling due to the interaction between the orbital characteristics of S-NPP (and other polar-orbiting platforms) and timescales of dust transport and synoptic scale weather patterns.

5 Summary and Conclusions

We presented a methodology for developing nonspherical dust optical models based on AERONET inversion data for use in the SOAR algorithm that will create the Version 1 VIIRS Deep Blue aerosol data product, which is planned to be released to the public in late 2017. These models can be used for other aerosol remote sensing or modeling purposes as well. We account for nonsphericity of dust particles by incorporating the same spheroid shape distribution as used in the AERONET inversion algorithm when integrating the optical properties of the single particle database used in this development. By doing so, the consistency between the aerosol optical models and sky radiances observed by AERONET could be preserved.

Considering the significant contribution of Saharan dust over the global ocean, we use the coarse-mode dust optical model optimized for the Capo Verde site combined with the weakly absorbing fine-mode model, for the initial data processing. It was found that the dust optical model, although optimized for a specific site, is representative for dust from various source regions, showing intermediate properties of them. Preliminary validation against AERONET direct-Sun observations (independent from the inversions used to develop the

optical model) suggested that the new dust optical model effectively mitigates the artificial scattering angle dependence of AOD (and AE) found when spherical dust is assumed, resulting in significant improvements in comparison statistics except for median bias. The similar median bias between spherical and spheroidal models implied that climatological data from spherical assumption might be as useful as those from more advanced spheroidal assumption. However, it was revealed that there was still noticeable difference between the two in monthly mean data sets. Although averaging for a longer-term period might reduce the difference further, it also limits applications due to the averaging of the temporal signature of dust storms. Thus, the spheroidal assumption is superior in a climatological sense as well. In addition to AOD, the spheroidal model reduces the bias in AE (or FMF), which has implications for scientific applications where aerosol size information is of importance.

The scattering angle dependence of AOD also caused an artificial spatial pattern, which was improved when considering spheroidal model, in daily and monthly AOD maps. The improvement is expected to contribute to more accurate quantification of dust transport with the VIIRS' broad (3,040 km) swaths.

Since present approach is limited by the availability of AERONET inversion data, it is not trivial to create optical models for the dust sources that are not well-sampled by AERONET (e.g. Namib/Kalahari deserts, central Australia, Patagonia, Alaska). Thus, future attention to these regions is desired to achieve more complete set of dust optical models over the globe.

Although this study only focused on implementing the dust optical models in the VIIRS SOAR algorithm, ongoing development of the Deep Blue land algorithm also shows promising results when incorporating similar optical models. More tests are underway to find an optimal utilization of the new optical models in the land algorithm. With the inclusion of data over water surfaces, improved performance, and wider swath than MODIS, the VIIRS Deep Blue product suite will provide an enhanced view of global aerosol properties.

Acknowledgments

References

Ångström A. On the atmospheric transmission of Sun radiation and on dust in the air. Geogr Ann. 1929; 11:156–166.

Alam K, Trautmann T, Blaschke T. Aerosol optical properties and radiative forcing over mega-city Karachi. Atmos Res. 2011; 101:773–782. DOI: 10.1016/j.atmosres.2011.05.007

Banks JR, Brindley HE, Stenchikov G, Schepanski K. Satellite retrievals of dust aerosol over the Red Sea, 2005–2015. Atmos Chem Phys Discuss. 2016; doi: 10.5194/acp-2016-871

Bohren, CF., Huffman, DR. Absorption and Scattering of Light by Small Particles. Wiley; New York: 1983.

Bi L, Yang P, Kattawar GW, Kahn R. Single-scattering properties of triaxial ellipsoidal particles for a size parameter range from the Rayleigh to geometric-optics regimes. Appl Opt. 2009; 48:114–126. DOI: 10.1364/AO.48.000114 [PubMed: 19107180]

Buchard V, da Silva AM, Colarco PR, Darmenov A, Randles CA, Govindaraju R, Torres O, Campbell J, Spurr R. Using the OMI aerosol index and absorption aerosol optical depth to evaluate the NASA MERRA Aerosol Reanalysis. Atmos Chem Phys. 2015; 15:5743–5760. DOI: 10.5194/acp-15-5743-2015

Chin M, et al. Multi-decadal aerosol variations from 1980 to 2009: a perspective from observations and a global model. Atmos Chem Phys. 2014; 14:3657–3690. DOI: 10.5194/acp-14-3657-2014

Colarco PR, Kahn RA, Remer LA, Levy RC. Impact of satellite viewing-swath width on global and regional aerosol optical thickness statistics and trends. Atmos Meas Tech. 2014; 7:2313–2335. DOI: 10.5194/amt-7-2313-2014

Cziczo DJ, Froyd KD, Hoose C, Jensen EJ, Diao M, Zondlo MA, Smith JB, Twohy CH, Murphy DM. Clarifying the Dominant Sources and Mechanisms of Cirrus Cloud Formation. Science. 2013; 340:1320–1324. DOI: 10.1126/science.1234145 [PubMed: 23661645]

Draine BT, Flatau PJ. Discrete-dipole approximation for scattering calculations. J Opt Soc Am A. 1994; 11:1491–1499. DOI: 10.1364/JOSAA.11.001491

Dubovik O, King MD. A flexible inversion algorithm for retrieval of aerosol optical properties from Sun and sky radiance measurements. J Goephys Res. 2000; 105:20673–20696. DOI: 10.1029/2000JD900282

Dubovik O, Smirnov A, Holben BN, King MD, Kaufman YJ, Eck TF, Slutsker I. Accuracy assessments of aerosol optical properties retrieved from Aerosol Robotic Network (AERONET) Sun and sky radiance measurements. J Geophys Res. 2000; 105:9791–9806. DOI: 10.1029/2000JD900040

Dubovik O, Holben B, Eck TF, Smirnov A, Kaufman YJ, King MD, Tanre D, Slutsker I. Variability of absorption and optical properties of key aerosol types observed in worldwide locations. J Atmos Sci. 2002; 59:590–608. 10.1175/1520-0469(2002)059<0590:VOAAOP>2.0.CO;2.

Dubovik O, et al. Application of spheroid models to account for aerosol particle nonsphericity in remote sensing of desert dust. J Geophys Res. 2006; 111:D11208.doi: 10.1029/2005JD006619

Eck TF, Holben BN, Reid JS, Dubovik O, Smirnov A, O'Neill NT, Slutsker I, Kinne S. Wavelength dependence of the optical depth of biomass burning, urban, and desert dust aerosols. J Geophys Res. 1999; 104:31333–31349. DOI: 10.1029/1999JD900923

Eck TF, et al. Spatial and temporal variability of column-integrated aerosol optical properties in the southern Arabian Gulf and United Arab Emirates in summer. J Geophys Res. 2008; 113:D01204.doi: 10.1029/2007JD008944

Eck TF, et al. Climatological aspects of the optical properties of fine/coarse mode aerosol mixtures. J Geophys Res. 2010; 115:D19205.doi: 10.1029/2010JD014002

Egan, WG., Hilgeman, TW. Optical properties of inhomogeneous materials: applications to geology astronomy chemistry and engineering. Academic Press; NewYork: 1979.

Feng Q, Yang P, Kattawar GW, Hsu CN, Tsay SC, Laszlo I. Effects of particle nonsphericity and radiation polarization on retrieving dust properties from MODIS observations. J Aerosol Sci. 2009; 40:776–789. DOI: 10.1016/j.jaerosci.2009.05.001

Gillespie JB, Lindberg JD. Ultraviolet and visible imaginary refractive index of strongly absorbing atmospheric particulate matter. Appl Opt. 1992; 31:2112–2115. [PubMed: 20720866]

Giorgi F. A particle dry-deposition parameterization scheme for use in tracer transport models. J Geophys Res. 1986; 91:9794–9806. DOI: 10.1029/JD091iD09p09794

Hansen JE, Travis LD. Light scattering in planetary atmospheres. Space Sci Rev. 1974; 16:527–610.

Hess M, Koepke P, Schult I. Optical properties of aerosols and clouds: The software package OPAC. Bull Am Met Soc. 1998; 79:831–944. DOI: 10.1175/1520-0477(1998)079

Holben BN, et al. AERONET–A federated instrument network and data archive for aerosol characterization. Remote Sens Environ. 1998; 66:1–16. DOI: 10.1016/S0034-4257(98)00031-5

Holben BN, Eck TF, Slustker I, Smirnov A, Sinyuk A, Shafer J, Giles D, Dubovik O. AERONET's version 2.0 quality assurance criteria. Proc SPIE. 2006; 6408:64080Q.doi: 10.1117/12.706524

Hsu NC, Tsay SC, King MD, Herman JR. Aerosol properties over bright-reflecting source regions. IEEE Trans Geosci Remote Sens. 2004; 42:557–569. DOI: 10.1109/TGRS.2004.824067

Hsu NC, Tsay SC, King MD, Herman JR. Deep blue retrievals of Asian aerosol properties during ACE-Asia. IEEE Trans Geosci Remote Sens. 2006; 44:3180–3195. DOI: 10.1109/TGRS. 2006.879540

Hsu NC, Jeong MJ, Bettenhausen C, Sayer AM, Hansell R, Seftor CS, Huang J, Tsay SC. Enhanced Deep Blue aerosol retrieval algorithm: The second generation. J Geophys Res Atmos. 2013; 118:9296–9315. DOI: 10.1002/jgrd.50712

Kahn R, West R, McDonald D, Rheingans B, Mishchenko MI. Sensitivity of multiangle remote sensing observations to aerosol sphericity. J Geophys Res. 1997; 102:16861–16870. DOI: 10.1029/96JD01934

Kaufman YJ, Tanré D, Boucher O. A satellite view of aerosols in the climate system. Nature. 2002; 419:215–223. DOI: 10.1038/nature01091 [PubMed: 12226676]

Kemppinen O, Nousiainen T, Merikallio S, Räisänen P. Retrieving microphysical properties of dust-like particles using ellipsoids: the case of refractive index. Atmos Chem Phys. 2015; 15:11117–11132. DOI: 10.5194/acp-15-11117-2015

Kok JF. Does the size distribution of mineral dust aerosols depend on the wind speed at emission? Atmos Chem Phys. 2011; 11:10149–10156. DOI: 10.5194/acp-11-10149-2011

Lee J, Kim J, Yang P, Hsu NC. Improvement of aerosol optical depth retrieval from MODIS spectral reflectance over the global ocean using new aerosol models archived from AERONET inversion data and tri-axial ellipsoidal dust database. Atmos Chem Phys. 2012; 12:7087–7102. DOI: 10.5194/acp-12-7087-2012

Lee J, Kim J, Lee YG. Simultaneous retrieval of aerosol properties and clear-sky direct radiative effect over the global ocean from MODIS. Atmos Environ. 2014; 92:309–317. DOI: 10.1016/j.atmosenv. 2014.04.021

Levy RC, Remer LA, Tanré D, Kaufman YJ, Ichoku C, Holben BN, Livingston JM, Russell PB, Maring H. Evaluation of the Moderate-Resolution Imaging Spectroradiometer (MODIS) retrievals of dust aerosol over the ocean during PRIDE. J Geophys Res. 2003; 108doi: 10.1029/2002JD002460

Levy RC, Remer LA, Kaufman YJ. Effects of neglecting polarization on the MODIS aerosol retrieval over land. IEEE Trans Geosci Remote Sens. 2004; 42(11):2576–2583. DOI: 10.1109/TGRS. 2004.837336

Li F, Vogelmann AM, Ramanathan V. Saharan dust aerosol radiative forcing measured from space. J Clim. 2004; 17:2558–2571. doi: 10.1175/1520-0442(2004)017<2558:SDARFM>2.0.CO;2.

Liao H, Seinfeld JH. Radiative forcing by mineral dust aerosols: sensitivity to key variables. J Geophys Res. 1998; 103:31637–31645. DOI: 10.1029/1998JD200036

Lin JJ, Noll KE, Holsen TM. Dry deposition velocities as a function of particle-size in the ambient atmosphere. Aerosol Sci Tech. 1994; 20:239–252. DOI: 10.1080/02786829408959680

Masuda K, Mano Y, Ishimoto H, Tokuno M, Yoshizaki Y, Okawara N. Assessment of the nonsphericity of mineral dust from geostationary satellite measurements. Remote Sens Environ. 2002; 82:238–247. DOI: 10.1016/S0034-4257(02)00040-8

Meng Z, Yang P, Kattawar GW, Bi L, Liou KN, Laszlo I. Single-scattering properties of tri-axial ellipsoidal mineral dust aerosols: A database for application to radiative transfer calculations. J Aerosol Sci. 2010; 41:501–512. DOI: 10.1016/j.jaerosci.2010.02.008

Mishchenko MI I, Geogdzhayev V, Liu L, Ogren JA, Lacis AA, Rossow WB, Hovenier JW, Volten H, Muñoz O. Aerosol retrievals from AVHRR radiances: effects of particle nonsphericity and absorption and an updated long-term global climatology of aerosol properties. J Quant Spectrosc Ra. 2003; 75-80:953–972. DOI: 10.1016/S0022-4073(02)00331-X

Mishchenko MI, Travis LD. T-matrix computations of light-scattering by large spheroidal particles. Opt Commun. 1994; 109:16–21. DOI: 10.1016/0030-4018(94)90731-5

Mishchenko MI, Travis LD, Kahn RA, West RA. Modeling phase functions for dustlike tropospheric aerosols using a shape mixture of randomly oriented polydisperse spheroids. J Geophys Res. 1997; 102:16831–16847. DOI: 10.1029/96JD02110

O'Neill NT, Eck TF, Smirnov A, Holben BN, Thulasiraman S. Spectral discrimination of coarse and fine mode optical depth. J Geophys Res. 2003; 108doi: 10.1029/2002JD002975

Remer LA, Kaufman YJ, Tanré D, Mattoo S, Chu DA, Martins JV, Li RR, Ichoku C, Levy RC, Kleidman RG, Eck TF, Vermote E, Holben BN. The MODIS aerosol algorithm, products and validation. J Atmos Sci. 2005; 62:947–973. DOI: 10.1175/JAS3385.1

Sayer AM, Hsu NC, Bettenhausen C, Jeong MJ, Holben BN, Zhang J. Global and regional evaluation of over-land spectral aerosol optical depth retrievals from SeaWiFS. Atmos Meas Tech. 2012a; 5:1761–1778. DOI: 10.5194/amt-5-1761-2012

Sayer AM, Hsu NC, Bettenhausen C, Ahmad Z, Holben BN, Smirnov A, Thomas GE, Zhang J. SeaWiFS Ocean Aerosol Retrieval (SOAR): Algorithm, validation, and comparison with other data sets. J Geophys Res. 2012b; 117:D03206.doi: 10.1029/2011JD016599

Sayer AM, Hsu NC, Bettenhausen C, Jeong MJ. Validation and uncertainty estimates for MODIS Collection 6 "Deep Blue" aerosol data. J Geophys Res Atmos. 2013; 118:7864–7872. DOI: 10.1002/jgrd.50600

Sayer AM, Munchak LA, Hsu NC, Levy RC, Bettenhausen C, Jeong MJ. MODIS Collection 6 aerosol products: Comparison between Aqua's e-Deep Blue, Dark Target, and "merged" data sets, and usage recommendations. J Geophys Res Atmos. 2014; 119:13965–13989. DOI: 10.1002/2014JD022453

Sayer AM, Hsu NC, Bettenhausen C, Jeong MJ, Meister G. Effect of MODIS Terra radiometric calibration improvements on Collection 6 Deep Blue aerosol products: Validation and Terra/Aqua consistency. J Geophys Res Atmos. 2015; 120:12,157–12,174. DOI: 10.1002/2015JD023878

Sayer AM, Hsu NC, Bettenhausen C, Holz RE, Lee J, Quinn G, Veglio P. Cross-calibration of S-NPP VIIRS moderate-resolution reflective solar bands against MODIS Aqua over dark water scenes. Atmos Meas Tech. 2017; 10:1425–1444. DOI: 10.5194/amt-10-1425-2017

Scarnato BV, China S, Nielsen K, Mazzoleni C. Perturbations of the optical properties of mineral dust particles by mixing with black carbon: a numerical simulation study. Atmos Chem Phys. 2015; 15:6913–6928. DOI: 10.5194/acp-15-6913-2015

Schuster GL, Dubovik O, Arola A. Remote sensing of soot carbon – Part 1: Distinguishing different absorbing aerosol species. Atmos Chem Phys. 2016; 16:1565–1585. DOI: 10.5194/acp-16-1565-2016

Smirnov A, Holben BN, Eck TF, Dubovik O, Slutsker I. Cloud-screening and quality control algorithms for the AERONET database. Remote Sens Environ. 2000; 73:337–349. DOI: 10.1016/S0034-4257(00)00109-7

Smith AJA, Grainger RG. Does variation in mineral composition alter the short-wave light scattering properties of desert dust aerosol? J Quant Spectrosc Ra. 2014; 133:235–243. DOI: 10.1016/j.jqsrt.2013.08.005

Sokolik IN, Toon OB. Incorporation of mineralogical composition into models of the radiative properties of mineral aerosol from UV to IR wavelengths. J Geophys Res. 1999; 104:9423–9444.

Spurr R. VLIDORT: A linearized pseudo-spherical vector discrete ordinate radiative transfer code for forward model and retrieval studies in multilayer multiple scattering media. J Quant Spectrosc Ra. 2006; 102:316–342. DOI: 10.1016/j.jqsrt.2006.05.005

Sugimoto N, Nishizawa T, Shimizu A, Matsui I, Kobayashi H. Detection of internally mixed Asian dust with air pollution aerosols using a polarization optical particle counter and a polarization-sensitive two-wavelength lidar. J Quant Spectrosc Ra. 2015; 150:107–113. DOI: 10.1016/j.jqsrt.2014.08.003

Tegen I, Hollrig P, Chin M, Fung I, Jacob D, Penner J. Contribution of different aerosol species to the global aerosol extinction optical thickness: Estimates from model results. J Geophys Res. 1997; 102:23895–23915. DOI: 10.1029/97JD01864

Wagner R, Ajtai T, Kandler K, Lieke K, Linke C, Müller T, Schnaiter M, Vragel M. Complex refractive indices of Saharan dust samples at visible and near UV wavelengths: a laboratory study. Atmos Chem Phys. 2012; 12:2491–2512. DOI: 10.5194/acp-12-2491-2012

Waterman PC. Symmetry, unitarity, and geometry in electromagnetic scattering. Phys Rev D. 1971; 3:825–839.

Wang J, Liu X, Christopher SA, Reid JS, Reid E, Maring H. The effects of non-sphericity on geostationary satellite retrievals of dust aerosols. Geophys Res Lett. 2003; 30doi: 10.1029/2003GL018697

Yang P, Liou KN. Light scattering by hexagonal ice crystals: comparison of finite-difference time domain and geometric optics models. J Opt Soc Am A. 1995; 12:162–176. DOI: 10.1364/JOSAA. 12.000162

Yang P, Liou K. Finite-difference time domain method for light scattering by small ice crystals in three-dimensional space. J Opt Soc Am A. 1996; 13:2072–2085. DOI: 10.1364/JOSAA.13.002072

Yang P, Liou KN, Mishchenko MI, Gao BC. Efficient finite-difference time domain scheme for light scattering by dielectric particles: application to aerosols. Appl Opt. 2000; 39:3727–3737. [PubMed: 18349948]

Yang P, Feng Q, Hong G, Kattawar GW, Wiscombe WJ, Mishchenko MI, Dubovik O, Laszlo I, Sokolik IN. Modeling of the scattering and radiative properties of nonspherical dust-like aerosols. J Aerosol Sci. 2007; 38:995–1014. DOI: 10.1016/j.jaerosci.2007.07.001

Yee SK. Numerical solution of initial boundary value problems involving Maxwell's equations in isotropic media. IEEE Trans Antennas Propag. 1966; 14:302–307.

Yin Y, Wurzler S, Levin Z, Reisin TG. Interactions of mineral dust particles and clouds: Effects on precipitation and cloud optical properties. J Geophys Res. 2002; 107doi: 10.1029/2001JD001544

Yoshioka M, Mahowald NM, Conley AJ, Collins WD, Fillmore DW, Zender CS, Coleman DB. Impact of desert dust radiative forcing on Sahel precipitation: Relative importance of dust compared to sea surface temperature variations, vegetation changes, and greenhouse gas warming. J Clim. 2007; 20:1445–1467. DOI: 10.1175/JCLI4056.1

Yu H, Remer LA, Kahn RA, Chin M, Zhang Y. Satellite perspective of aerosol intercontinental transport: From qualitative tracking to quantitative characterization. Atmos Res. 2013; 124:73–100. DOI: 10.1016/j.atmosres.2012.12.013

Yurkin MA V, Maltsev P, Hoekstra AG. The discrete dipole approximation for simulation of light scattering by particles much larger than the wavelength. J Quant Spectrosc Ra. 2007; 106:546–557. DOI: 10.1016/j.jqsrt.2007.01.033

Key Points

- AERONET-based nonspherical dust optical property model for use in NASA's VIIRS Deep Blue/SOAR over-water algorithm

- Significant improvements in SOAR aerosol product over dust layers

- Enhanced view of global aerosol properties by VIIRS Deep Blue algorithm suite
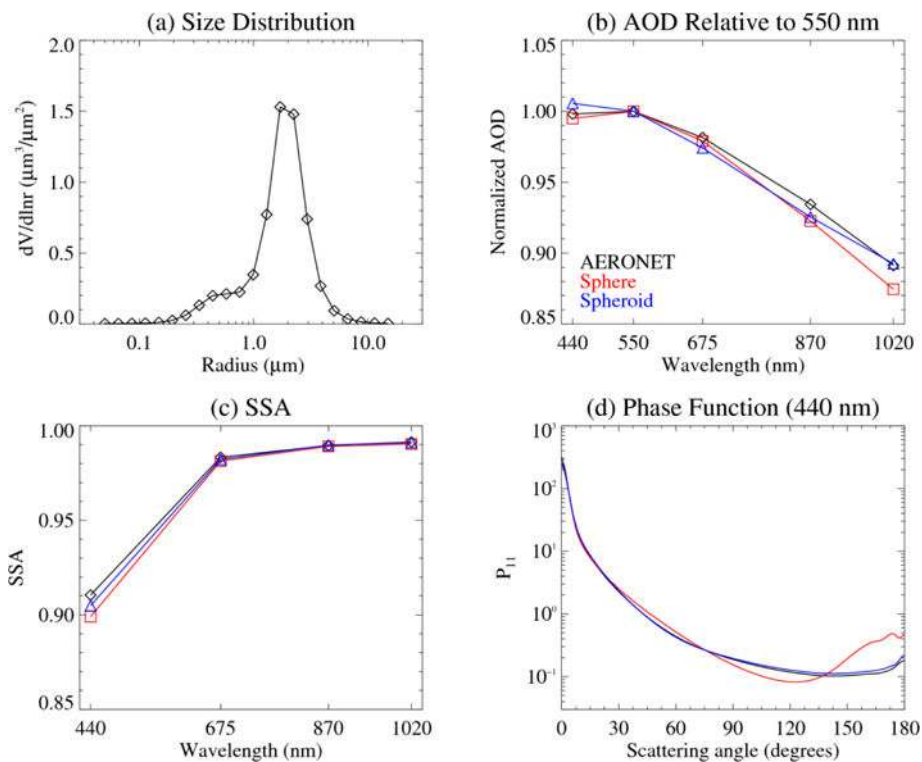
Figure 1.
(a) AERONET size distribution, (b) spectral AOD relative to 550 nm, (c) spectral SSA, and
(d) phase function at 440 nm for a dust case observed at Capo Verde at 10:24 a.m. UTC, 9
March 2006. Aerosol optical properties derived from the single-scattering property database
are superimposed in (b-d) for spherical (red) and spheroidal (blue) models.
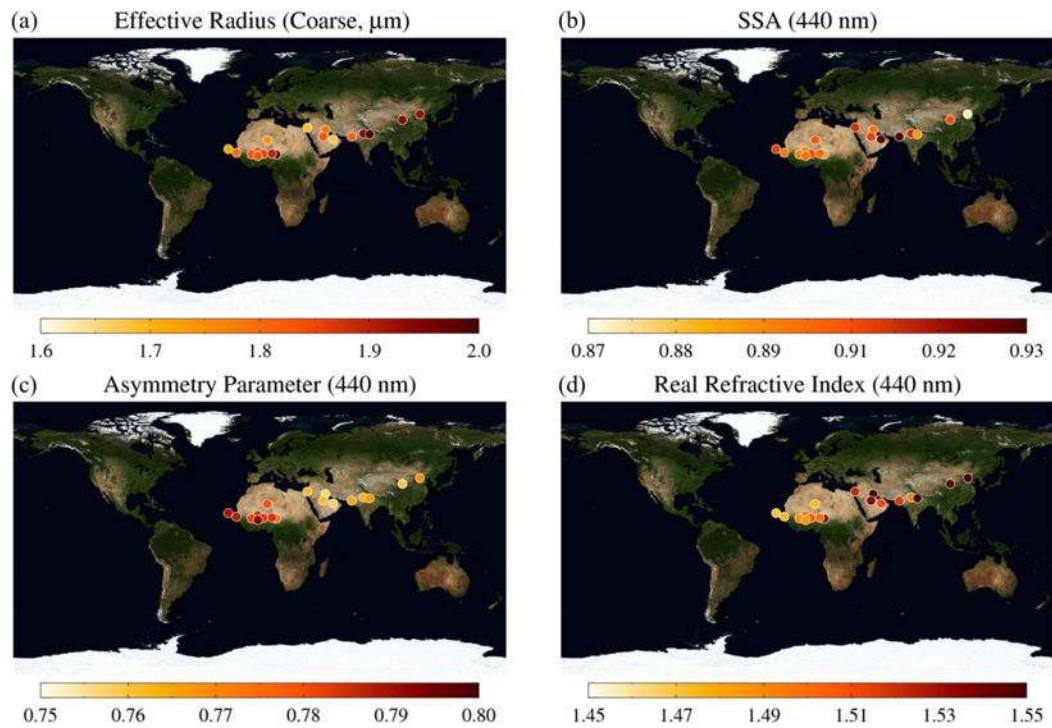
Figure 2.
Median (a) effective radius (coarse-mode), (b) SSA, (c) asymmetry parameter, and (d) the real part of the refractive index of dust-dominated aerosols derived from AERONET inversion data over various locations. Values in (b-d) are for 440 nm. Sites are shown only if the number of data points that meet the requirement for dust-dominated case (discussed in the text) is higher than 30.
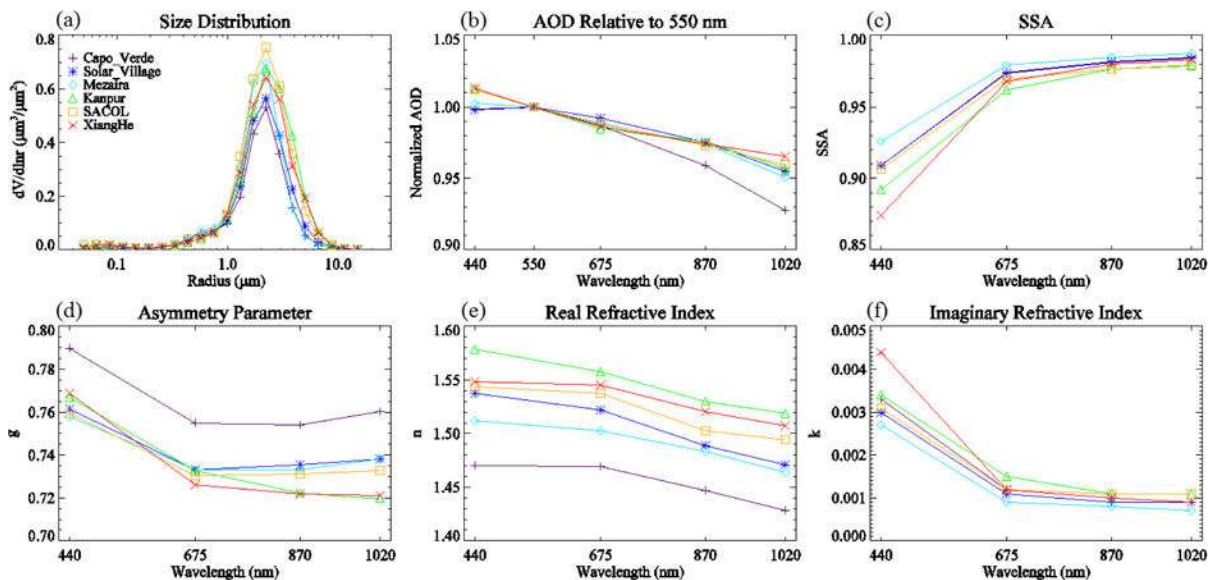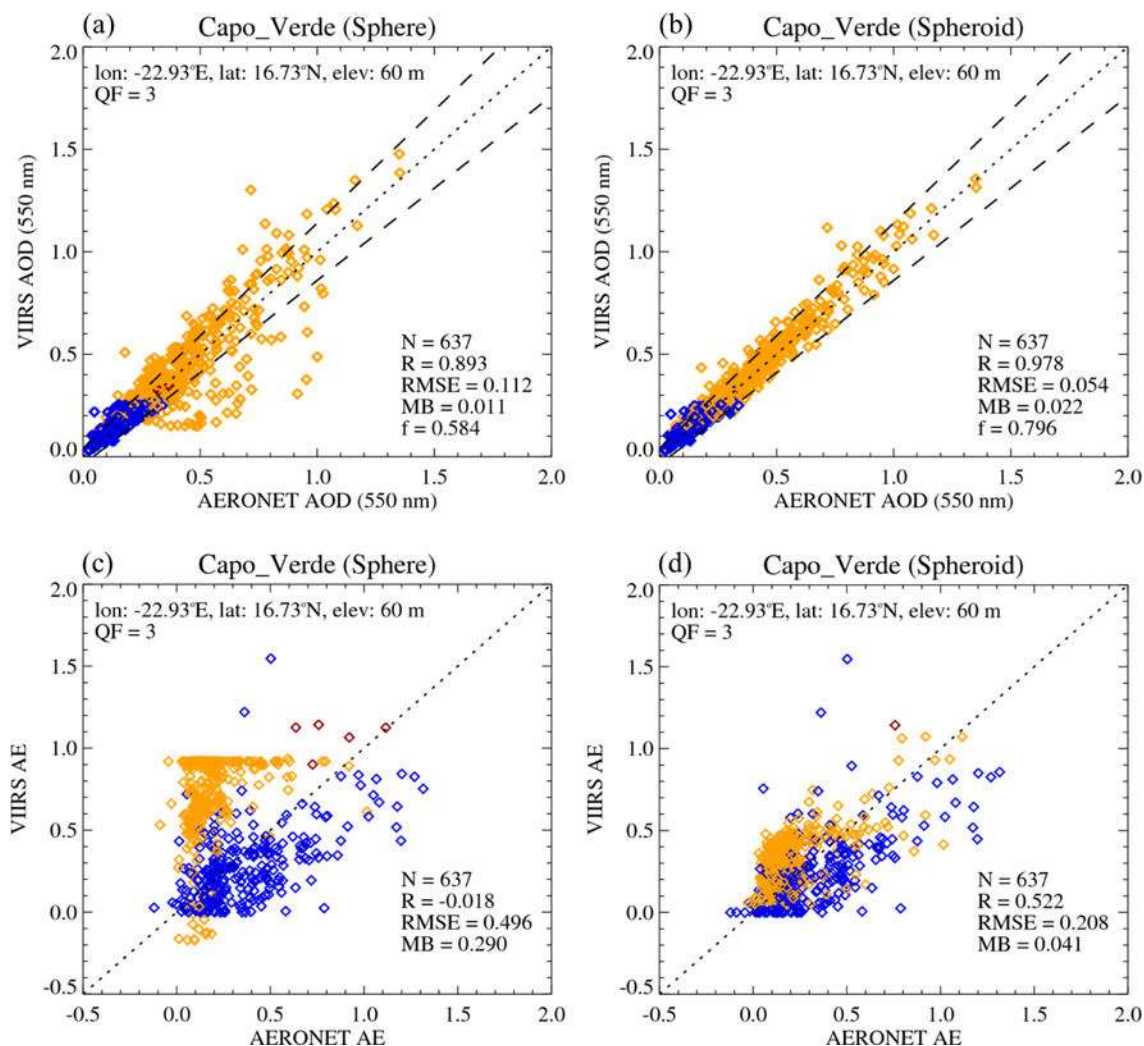
Figure 3.
AERONET-derived median (a) size distribution, (b) spectral AOD relative to 550 nm, (c)
SSA, (d) asymmetry parameter, and (e) real and (f) the imaginary part of the refractive index
for dust-dominated aerosols at six locations influenced by different source regions.
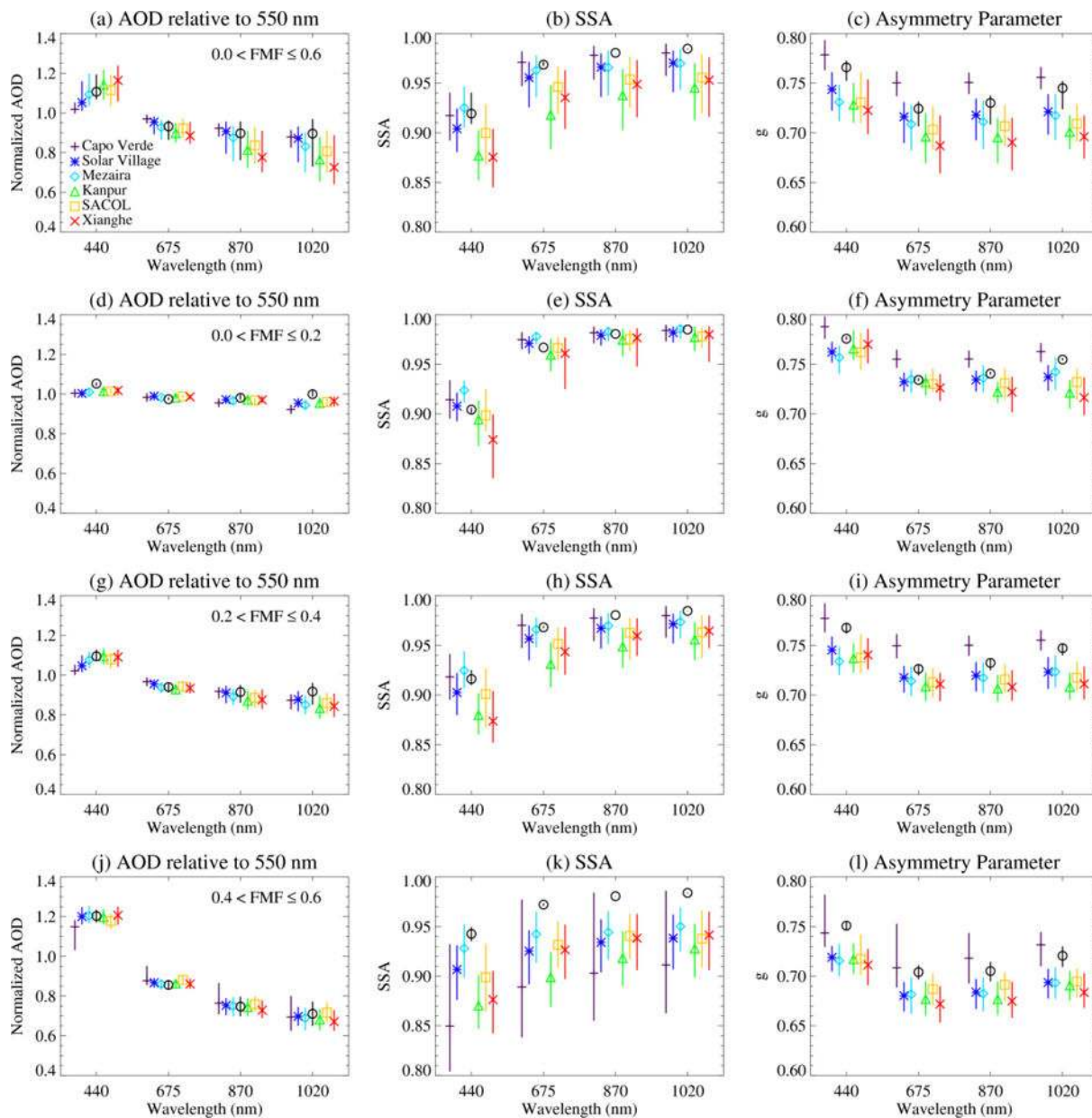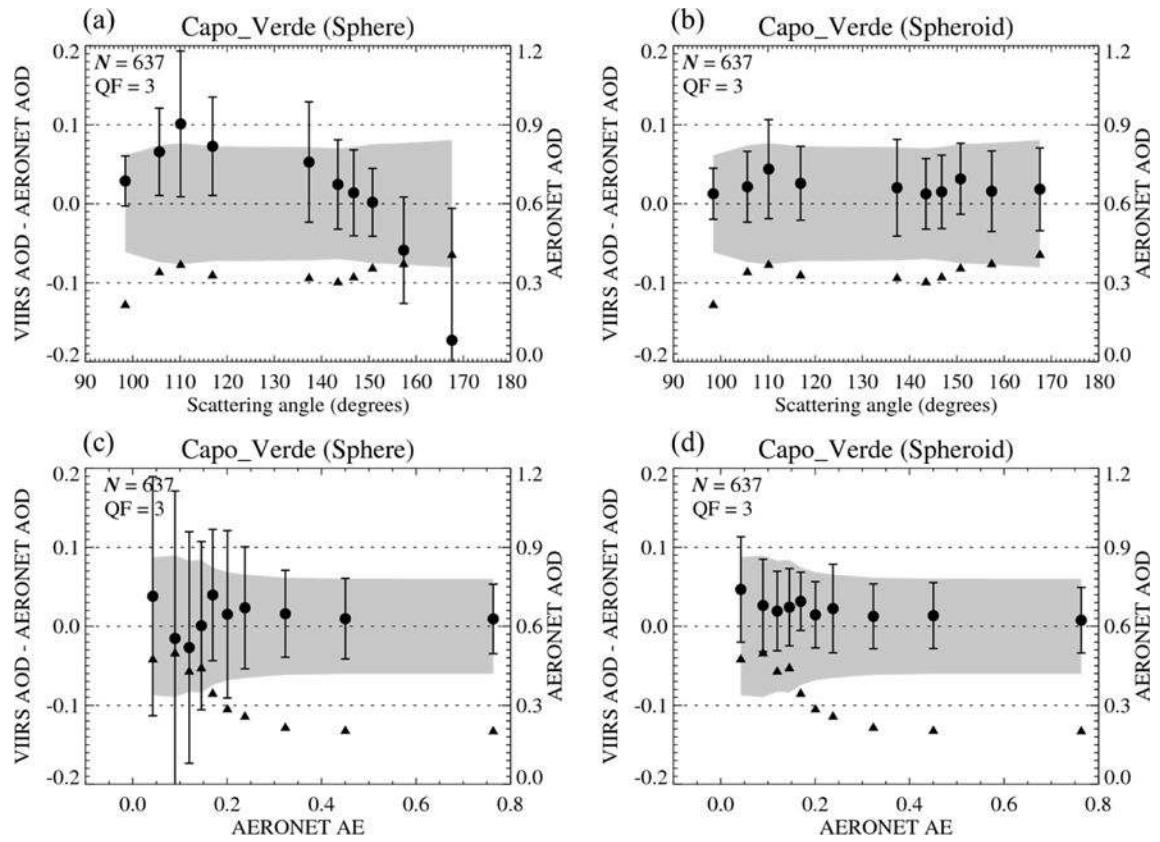
Figure 4.
AERONET (colored symbols) and dust optical model derived (black symbol) spectral AOD
relative to 550 nm (left), SSA (middle), and asymmetry parameter (right) for different FMF
ranges: (a-c) 0.0 < FMF ≤0.6, (d-f) 0.0 < FMF ≤0.2, (g-i) 0.2 < FMF ≤0.4, and (j-l) 0.4 <
FMF ≤0.6. AERONET data are for Capo Verde (purple), Solar Village (blue), Mezaira
(cyan), Kanpur (green), SACOL (yellow), and Xianghe (red) sites. Note that the colored
symbols are purposely offset along the x-axis for a clear illustration, and do not imply actual
differences in wavelength. Median and central 68% interval are shown.

Figure 5.
Scatter plots of (a, b) AOD at 550 nm and (c, d) AE between AERONET and VIIRS SOAR at Capo Verde from March 2012 to December 2016. SOAR results are shown assuming (a, c) spherical and (b, d) spheroidal dust optical models. Colors represent the best-fit aerosol optical model determined by SOAR for each case; dust is in yellow, marine in blue, and fine-dominated (rare for this site) in red. For AOD comparisons, dashed lines show the expected error interval.
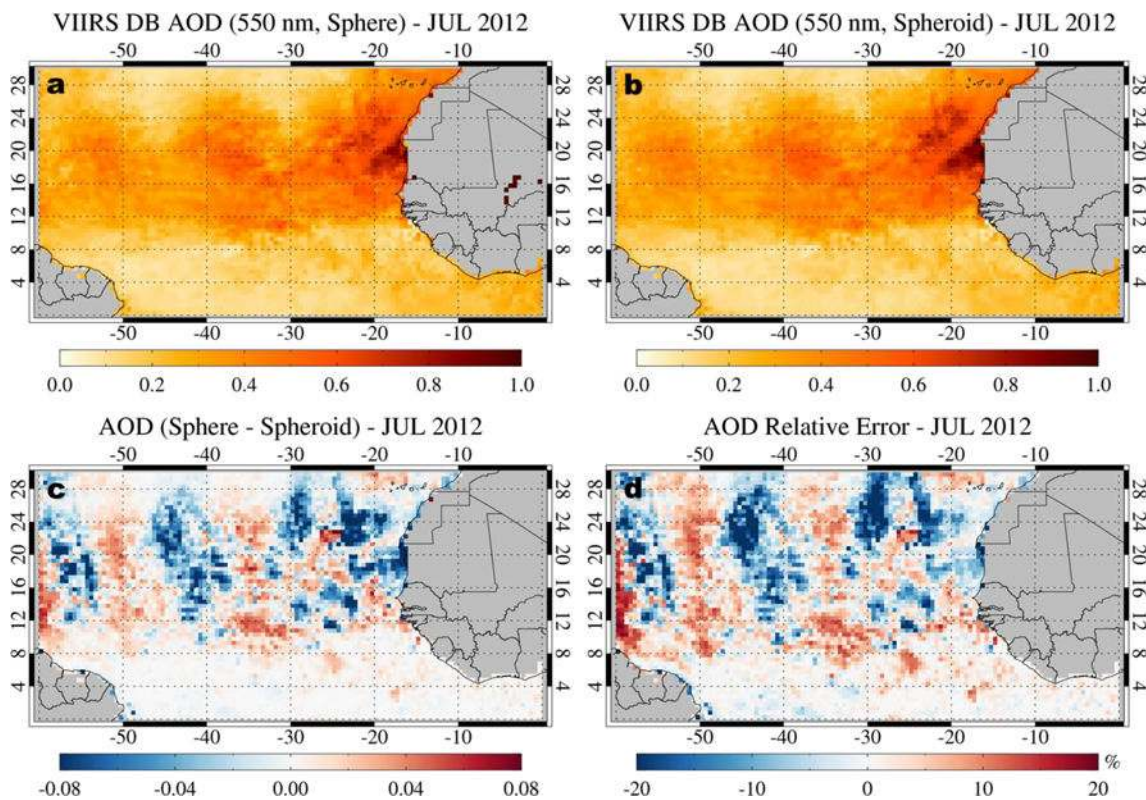
Figure 6.
Mean and standard deviation of AOD errors in SOAR retrievals at Capo Verde site as a function of (a, b) scattering angle and (c, d) AE for (a, c) spherical and (b, d) spheroidal dust optical models. Data in 10 equal-number-of-data bins are shown with mean AERONET AOD in triangle (corresponding to the right y-axis). Shaded area is the expected error envelope for the mean AOD.
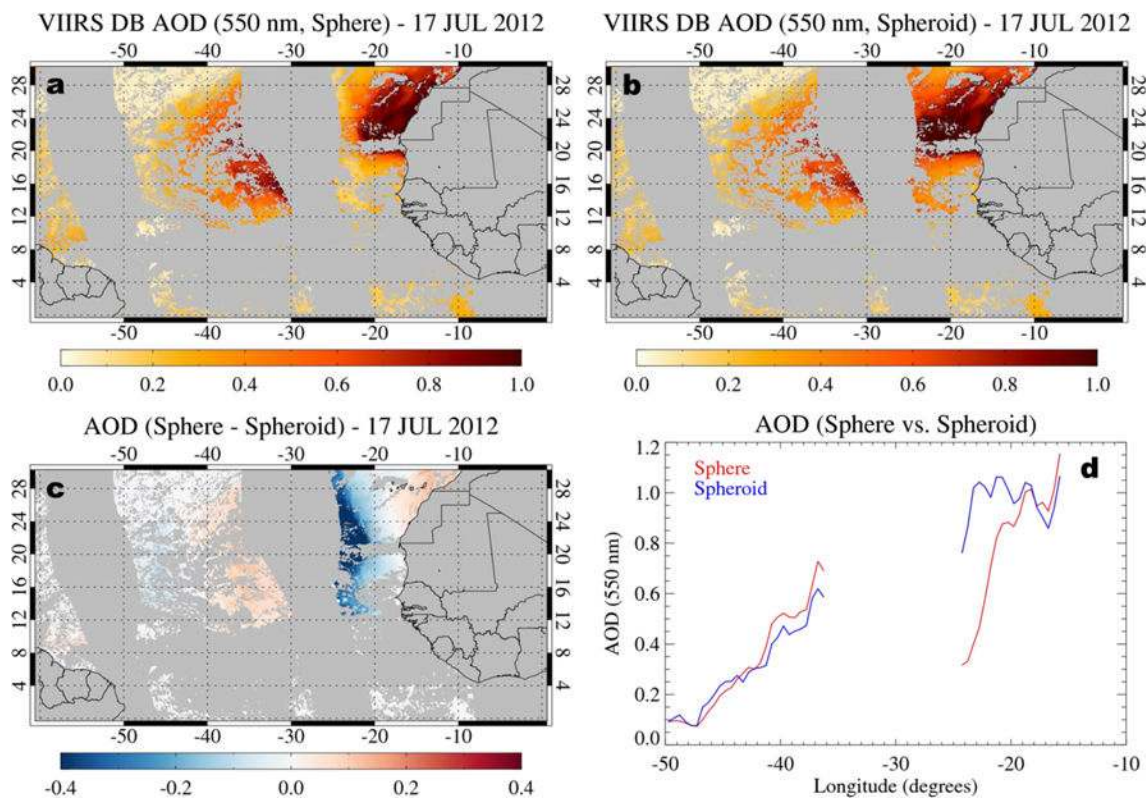
Figure 7.
SOAR AOD map using (a) spherical and (b) spheroidal dust optical models for a Saharan dust event on 17 July 2012, (c) AOD difference (spherical – spheroidal), and (d) AOD longitudinal cross section from −50°E ~ −15°E at 23.75°N, for data gridded at 0.5° resolution.

Figure 8.
Monthly mean SOAR AOD maps from (a) spherical and (b) spheroidal dust optical models
over the Atlantic Ocean in July 2012, and the (c) absolute and (d) relative AOD error of the
spherical model as compared to the spheroidal model. The relative error is shown in
percentage. Data gridded at 0.5° resolution are shown.

Table 1

Median volume median radius (r$_v$), geometric standard deviation (σ), and real (n) and imaginary (k) part of the refractive index of coarse-mode dust optical models at six AERONET sites.

Site name	r$_v$ [μm]	σ μm	Refractive index (n+ik)			
			440 nm	675 nm	870 nm	1020 nm
Capo Verde	2.00	0.51	1.47+0.0033i	1.47+0.0012i	1.45+0.0010i	1.43+0.0009i
Solar Village	2.10	0.51	1.54+0.0030i	1.52+0.0011i	1.49+0.0009i	1.47+0.0009i
Mezaira	1.91	0.48	1.51+0.0027i	1.50+0.0009i	1.48+0.0008i	1.46+0.0007i
Kanpur	2.36	0.51	1.58+0.0034i	1.56+0.0015i	1.53+0.0011i	1.52+0.0011i
SACOL	2.20	0.50	1.54+0.0031i	1.54+0.0012i	1.50+0.0011i	1.49+0.0011i
Xianghe	2.23	0.52	1.55+0.0044i	1.55+0.0012i	1.52+0.0010i	1.51+0.0009i

Table 2

Same as Table 1, but for the fine-mode optical model.

Aerosol model	r_v [μm]	σ μm	Refractive index (n+ik)			
			440 nm	675 nm	870 nm	1020 nm
weakly absorbing	0.19	0.44	1.43+0.001i	1.43+0.001i	1.43+0.001i	1.43+0.001i

Table 3

Complex refractive index of fine- and coarse-mode dust optical models for VIIRS bands, used in SOAR version 1.

Size mode	Refractive index for SOAR band (n+ik)							
	488 nm	555 nm	672 nm	865 nm	1240 nm	1610 nm	2250 nm
Fine	1.43+0.001i	1.43+0.001i	1.43+0.001i	1.43+0.001i	1.41+0.001i	1.40+0.001i	1.38+0.001i
Coarse	1.54+0.0016i	1.54+0.00012i	1.54+0.0007i	1.54+0.0006i	1.49+0.0005i	1.48+0.0005i	1.47+0.0005i

Table 4

Comparison statistics of AOD between AERONET and VIIRS SOAR for spherical and spheroidal (in parentheses) dust models at Capo Verde, KAUST Campus, and Karachi. Statistics shown are the number of data points (N), Pearson coefficient (R), root-mean-squre error (RMSE), median bias (MB), and fraction within expected error (f). The expected error for AOD is defined as ±(0.03+10%). Data from March 2012 to December 2016 are used.

Site name	Location (latitude, longitude, elevation)	N	R	RMSE	MB	f
Capo Verde	16.73°N, −22.93°E, 60 m	637	0.89	0.11	0.01	0.58
			(0.98)	(0.05)	(0.02)	(0.80)
Gosan	33.29°N, 126.16°E, 72 m	290	0.91	0.10	0.03	0.48
			(0.91)	(0.10)	(0.02)	(0.49)
KAUST	22.31°N, 39.10°E, 11 m	511	0.89	0.15	0.03	0.57
			(0.98)	(0.07)	(0.03)	(0.76)
Karachi	24.87°N, 67.03°E, 49 m	374	0.76	0.16	0.01	0.42
			(0.90)	(0.13)	(−0.03)	(0.46)
Lampedusa	12.63°N, 35.52°E, 45 m	724	0.93	0.05	0.01	0.80
			(0.95)	(0.04)	(0.01)	(0.83)

Table 5

Same as Table 4 except for the case of AE, and note there is no expected error defined for AE.

Site name	Location (latitude, longitude, elevation)	N	R	RMSE	f
Capo Verde	16.73°N, −22.93°E, 60 m	637	−0.02	0.50	0.29
			(0.52)	(0.21)	(0.04)
Gosan	33.29°N, 126.16°E, 72 m	290	0.55	0.34	−0.04
			(0.59)	(0.32)	(−0.05)
KAUST	22.31°N, 39.10°E, 11 m	511	0.08	0.44	0.07
			(0.60)	(0.30)	(−0.11)
Karachi	24.87°N, 67.03°E, 49 m	374	0.48	0.37	0.07
			(0.80)	(0.24)	(−0.06)
Lampedusa	12.63°N, 35.52°E, 45 m	724	0.71	0.43	−0.21
			(0.80)	(0.39)	(−0.24)